OneQ: A Compilation Framework for Photonic One-Way Quantum Computation

Hezi Zhang
hezi@cs.ucsb.edu
University of California
Santa Barbara, USA

Anbang Wu
anbang@cs.ucsb.edu
University of California
Santa Barbara, USA

Yuke Wang
yuke_wang@cs.ucsb.edu
University of California
Santa Barbara, USA

Gushu Li
gushuli@ece.ucsb.edu
University of California
Santa Barbara, USA

Hassan Shapourian
hshapour@cisco.com
Cisco Quantum Lab
San Jose, USA

Alireza Shabani
ashabani@cisco.com
Cisco Quantum Lab
Sant Monica, USA

Yufei Ding
yufeiding@cs.ucsb.edu
University of California
Santa Barbara, USA

Abstract

In this paper, we propose OneQ, the first optimizing compilation framework for one-way quantum computation towards realistic photonic quantum architectures. Unlike previous compilation efforts for solid-state qubit technologies, our innovative framework addresses a unique set of challenges in photonic quantum computing. Specifically, this includes the dynamic generation of qubits over time, the need to perform all computation through measurements instead of relying on 1-qubit and 2-qubit gates, and the fact that photons are instantaneously destroyed after measurements. As pioneers in this field, we demonstrate the vast optimization potential of photonic one-way quantum computing, showcasing the remarkable ability of OneQ to reduce computing resource requirements by orders of magnitude.

CCS Concepts

• **Computer systems organization** → **Quantum computing**; • **Software and its engineering** → **Compilers**.

Keywords

one-way quantum computing, measurement-based quantum computing (MBQC), photonics, compiler

1 Introduction

Quantum computing (QC) is promising in providing significant speedup for many problems, such as large-number factorization [1], unordered database search [2] and simulation in quantum chemistry [3, 4]. Tremendous progress has been made in hardware technologies for quantum computing, including superconducting [5], ion trap [6], neutral atoms [7], and photonics [8], in both research lab settings and industrial production levels. With no clear winner among current platforms, it is expected that multiple technologies will continue to evolve together to meet diverse mission needs and application requirements.

In recent years, there has been a surge of interest in photonic quantum computing [9, 10], mainly due to the unique advantages of photonic qubits [11, 12], such as great scalability, long coherence time and easy integration with quantum networks. This interest is further fueled by the breakthroughs in photonic technologies [13, 14] and the successful demonstration of quantum supremacy on photonic quantum computers [15–17]. Moreover, PsiQuantum [18–20] recently announced the world's first manufacturing milestone for integrated quantum photonic chips, with quantum photonic and electronic chips being manufactured using advanced semiconductor tools.

However, photonic quantum computing also presents a unique set of features that cannot be directly handled by conventional programming and compiler frameworks [21, 22] for solid-state qubits. First, unlike the permanent qubits in solid-state systems [5–7], photonic qubits are flying qubits at the speed of light, and are generated dynamically over time. Second, in contrast to the solid-state platforms which entangle qubits by multi-qubit gates such as CNOT, entanglement between photonic qubits are more natively performed by projective measurements onto entangled states, a process referred to as *fusion* (e.g., simultaneous measurements in XX- and ZZ-bases project the qubits onto Bell states). Third, measurements on photonic qubits, including single-qubit measurements and fusions, instantaneously destroy the photons, meaning that each photonic qubit can be measured or fused at most once and cannot be reinitialized.

At programming level, measurement-based quantum computing (MBQC) [23] has been suggested as a native programming paradigm for photonic quantum computing, because it does not require long-lasting qubits or quantum gates, but only one-time measurements on qubits. Unlike the circuit model which initializes qubits to a product state of all $|0\rangle$s and performs algorithms by a sequence of gates that gradually creates entanglements, MBQC initializes qubits to an entangled state and performs algorithms by a pattern of single-qubit projective measurements (called *measurement pattern*) that gradually consumes the entanglements. During the computation, each qubit is measured only once and is then free to detach from the computing system or even disappear. This is why MBQC is also called "one-way" quantum computing (1WQC). In addition to MBQC, another popular programming paradigm for photonic quantum computing [15, 24] is the special-purpose model for Gaussian boson sampling [25], but it is not a universal computing model like MBQC and thus has restricted applications.

Yet few attempts have been made on the compilation side. While previous work [23, 26–28] has shown that the utilization of a lattice-like entangled state, i.e., a *cluster state*, can enable a basic interpreter from the circuit model to MBQC by joining the measurement patterns of individual gates on it, this approach is not efficient for scaling up on hardware. Practical photonic hardware scales up by first generating small entangled states (called *resource states*) and then combining them into larger entangled states through fusions [29]. Attempting to generate a large cluster state on such hardware would result in an unnecessarily significant fusion overhead, because a large amount of entanglements in the cluster state is actually redundant for the computation, but only to keep the lattice geometry. Instead of generating all entanglements of the cluster states, it is more efficient to only generate the entanglements required by the computation. Theses required entanglements can be represented by a non-lattice *graph state*, i.e. a generalized cluster state with arbitrary graph geometry. However, as the geometry of the graph state is irregular and varies depending on the specific program to be executed, it is not yet known how to efficiently map the irregular graph geometry onto an MBQC machine while complying with the hardware constraints.

In this paper, we investigate how to optimize the quantum program compilation for a photonic MBQC machine. As the first step, we abstract a *extendable space-time coupling graph* to formulate the hardware model. This coupling graph represents the hardware resources (e.g., resource state generators (RSG)) and constraints (e.g., available photon routing) in a way that suits the subsequent compilation designs. With this abstraction, we identify three key challenges in compiling graph states onto the hardware model. First, resource states are generated dynamically in layers over time by limited number of RSGs and thus cannot be available simultaneously. Second, there is no direct correspondence between a graph state node and a photonic qubit due to the lack of high-degree qubits in the resource states. Third, there is a mismatch between the irregular geometry of the graph state and the regular structure of fusion supports represented by the coupling graph. Additionally, for resource states of small size, there is a further constraint that non-planar graphs cannot be accommodated by resource states generated in the same layer since the number of possible fusions on each resource state is too limited.
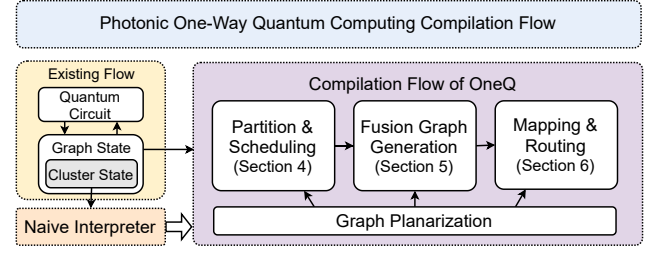

Figure 1: Framework Overview.

To this end, we propose an optimizing compilation framework consisting of three sequential stages (Figure 1), with each stage handled by a key module of the framework. The **Graph Partition and Scheduling** module (Section 4) partitions the graph state into subgraphs and schedules them onto resource states generated at different times. It achieves a balance between reducing the wait time of photons and increasing the potential efficiency of mapping by analyzing the dependencies among operations and considering the overall geometry. The **Fusion Graph Generation** module (Section 5) synthesizes the scheduled subgraphs by fusing low-degree qubits in the resource states into high-degree nodes in the graph and connecting them appropriately. The produced fusion strategy is agnostic to the coupling constraints, and is represented by a *fusion graph*. The **Fusion Mapping and Routing** module (Section 6) tackles the coupling constraints by finding an embedding layout of the irregular fusion graph into the regular coupling graph. Specifically, it makes the fusion graph compatible with the coupling graph by extending and routing the edges of the fusion graph along the edges of the coupling graph. By maximizing the compactness of the layout, we can reduce the number of required fusions, thus reducing the computation overhead and enhancing the overall fidelity. Lastly, the additional constraint for small resource states can be addressed by a planarity enforcement for all modules. With these modules and optimizations, our framework maximizes the utilization of computing resources and efficiently accommodates the irregularity and adaptivity of the graph states.

To summarize, our contributions in this paper are listed as below:

- We abstract a extendable space-time coupling graph to formulate the hardware model of a realistic photonic MBQC architecture.
- We identify three critical compilation challenges in the gap between MBQC programs and realistic photonic MBQC hardware, as well as an additional constraint in the cases of small resource states.
- We propose an optimizing compilation framework to efficiently deploy quantum programs onto the hardware, which includes three key optimization modules to tackle the identified challenges, along with a planarity enforcement process to address the additional constraint.
- Our framework outperforms the basic MBQC interpreter by orders of magnitude in terms of execution time and resource consumption of the compiled program.

2 Background and Related Work

2.1 MBQC on Photonic Platforms

Photonic qubits are an exceptional carrier of quantum information and are well-suited for the one-way model of quantum computing [30, 31]. The feasibility of photonic one-way quantum computing has been shown by implementing various quantum algorithms on photonic qubits in cluster states [32]. For example, Grover's algorithm was implemented on a 4-photon 4-qubit cluster state in [33] with a fidelity of 0.9, Deutsch-Jozsa algorithm was realized on a six-qubit cluster state in [34] with a fidelity of 0.96, and Simon's algorithm was performed on a five-qubit cluster state in [35] for a period-finding problem. Notably, rapid progress is being made toward scaling up the photonic platform with integrated waveguides and optical chips [36–42], and a fully reconfigurable optical processor has been demonstrated in [43].

Practical photonic hardware is scaled up by generating small-size resource states (e.g., three-qubit [29], four-qubit graph states [44]) and cascading them via fusion [45]. Fusion is a native operation in linear optics that projects a two-qubit state to an entangled state through joint measurements on the two qubits. For example, joint measurements in XX- and ZZ-basis projects two-qubit states onto Bell states. The joint measurements we use in this paper are in XZ- and ZX-basis, which merge two graph states to another graph state. As shown in Figure 2, the 3-qubit graph states ABC and DEF can be merged into a 4-qubit graph state $ABEF$ via a fusion on qubits C and D. The cost of each fusion is losing the two measured photons (qubit C and D in Fig. 2). In general, the fusion between an m-qubit graph state and an n-qubit graph state generates an $(m+n-2)$-qubit graph state, which is larger than the original graph states when $m, n > 2$.
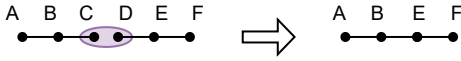

Figure 2: A fusion between graph states ABC and DEF. After the fusion between C and D, qubit C and D vanish while qubit A, B, E and F form a new graph state.

Despite facilitating scalability, fusions come with an overhead of losing two qubits each time and are the lowest-fidelity operations in the computing process. As a result, reducing the number of fusions is critical for reducing the required computing resources and enhancing the overall fidelity. Thus we consider it as one of essential optimization goals in our compilation framework, which is analogous to the goal of minimizing the number of CNOT gates in compilers for the circuit model.

2.2 Programming Paradigm of MBQC

2.2.1 MBQC Basics MBQC is a universal but conceptually distinct computational model from the circuit model, as computation in MBQC is driven by single-qubit projective measurements instead of 1-qubit and 2-qubit gates. The initial state used as the computing resource in MBQC can be a *graph state*, which is an entangled state of qubits located on a graph $G = (V, E)$, formally defined as the eigenstates of operator

$$s = X_i \bigotimes_{j \in n_i} Z_j, \quad \forall i \in V$$

where n_i is the set of neighboring qubits of $i \in V$. A graph state can be generated by preparing all qubits in $|+\rangle$ and applying a CZ gate on each pair of qubits connected by an edge $e \in E$. Given this graph state, computation can be driven by a pattern of Z-measurements and *equatorial measurements* $E(\alpha)$, i.e., measurements on the X-Y plane of Bloch sphere at an angle α. The graph G and the measurement basis of each qubit together form a *measurement pattern*.

MBQC has a classical-quantum hybrid nature in that it relies on a classical feed-forward to address the non-determinism of quantum measurement. Specifically, the state of unmeasured qubits are subjected to Pauli X- or Z-corrections according to the outcomes of the measured qubits. In practice, this can be implemented equivalently by adaptively adjusting the measurement bases of the remaining qubits, such that all corrections can be postponed to the end of the computation. As a result, these *adaptive measurements* induce dependencies between measurements. In particular, an $X^s Z^t$-correction with $s, t \in \{0, 1\}$ can be postponed by adjusting its measurement angle from α to $(-1)^s \alpha + t\pi$, i.e., $E(\alpha) X^s Z^t = E((-1)^s \alpha + t\pi)$. The dependencies in s and t are called X- and Z-dependency respectively.

There is a straightforward translation [46] from a circuit in the universal gate set $\{J(\alpha), CZ\}$ into a measurement pattern, because a measurement $E(\alpha)$ yielding an outcome $m \in \{0, 1\}$ is equivalent to a $J(\alpha)$ operator followed by a Z-measurement M_z yielding the same value, i.e., $E(\alpha) |\psi\rangle \rightarrow m$ corresponds to $M_z J(\alpha) |\psi\rangle \rightarrow m$,

$$J(\alpha) = \begin{bmatrix} 1 & e^{i\alpha} \\ 1 & -e^{i\alpha} \end{bmatrix}$$

For example, Figure 3 shows the translation from 3(a) to 3(b), with the measurement angles of qubits and the roles of being input or output marked on each of them. The 3-degree node a in 3(b) corresponds to the qubit A with 3 CZ gates in 3(a), while nodes b_1, b_2 correspond to single-qubit gates on qubit B (similarly for qubit C and D). Dependencies between measurements are represented by directed edges. For example, $b_1 \rightarrow b_2$ indicates that the measurement basis of b_2 may be adjusted according to the measurement outcome of b_1. This process can be rigorously described in ZX-calculus and optimized by available tools such as PyZX [47].
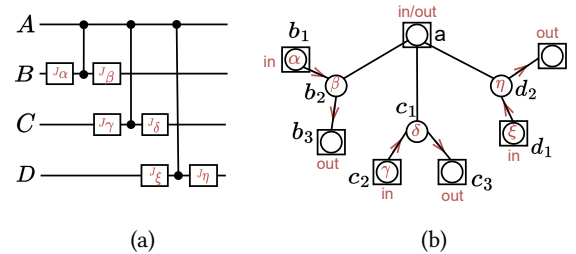

(a)   (b)

Figure 3: Translation from a circuit (a) to a graph state (b), with the measurement bases labeled on qubits. Qubits in (b) with 'in', 'out' or 'in/out' are input or output qubits. Arrows on the edges indicate the dependencies between measurements.

2.2.2 MBQC Interpreter While there has not been a compiler for practical MBQC machines, previous work on cluster states enables a basic interpreter from the circuit model to MBQC, which we adopt as the baseline approach in our evaluation.

Cluster states are universal for MBQC as it allows the implementation of a universal gate set, such as single-qubit gates along with CNOT. In particular, an arbitrary single-qubit gate can be implemented by a measurement pattern on a line of qubits in the cluster state, such as the red circles in Figure 4(b), while a CNOT gate can be implemented on two lines of qubits joined by a qubit in between, such as the green circles in Figure 4(b). The X, Y labels stand for X-, Y-basis, while ξ, η, ζ stand for the angles of general equatorial measurements. Measurements in bases except X, Y and Z are adaptive measurements and can thus induce dependency. These adaptive measurements only arise in the measurement patterns of non-Clifford gates, meaning that all Clifford gates can be executed simultaneously on the cluster state even if they are dependent in the circuit model. For more details about measurement patterns of different gates, please refer to [23].
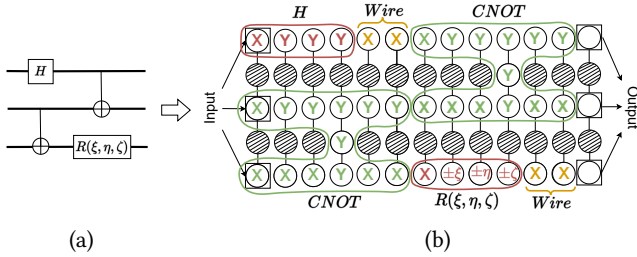

(a)   (b)

Figure 4: From a circuit (a) to an MBQC measurement pattern (b). Labels on the qubits stand for their measurement bases, with X, Y standing for X-,Y-basis, and ξ, η, ζ standing for the angles of equatorial measurements. Shaded qubits are redundant qubits which can be removed by Z-measurements.

A basic interpreter from the circuit model to MBQC can be constructed by simply joining the inputs and outputs of measurement patterns of those gates according to their positions in the circuit, as shown in Figure 4. Those measurement patterns can be aligned up by inserting identity gates, implemented by two adjacent X-measurements (or three adjacent Y-measurements), as shown by the yellow 'wires' in Figure 4(b). The qubits not used by measurement patterns of any gates are redundant to the computation, and can be removed by measurements in Z-basis (shaded qubits in Figure 4(b)). Similar to the circuit model compilation [48], CNOT gates on non-neighboring qubit strips can be implemented by inserting measurement patterns of SWAP gates whenever necessary. In this way, we can implement any quantum circuit in an MBQC manner. This interpreter greatly simplifies the mapping from qubits and gates in the circuit to the measurements on the cluster state. However, this approach is inefficient in the utilization of computing resources. Specifically, it makes many qubits redundant for computation and consumes their entanglements trivially by Z-measurements, without any regard for the huge overhead of generating those redundant entanglements on a practical MBQC machine.

3 Problem Formulation
3.1 Hardware Abstraction
Photonic hardware for one-way quantum computing involves three key stages: generation, routing, and measurement. In the first stage, an array of *resource state generators (RSG)* periodically produces copies of resource states, with the period referred to as a *clock cycle*. In the second stage, routers channel the resource states to different measurement locations using *spatial* and *temporal routing*. Spatial routing allows fusions between resource states generated by different RSGs, while temporal routing allows fusions between resource states generated at different times using *delay lines*, which can delay the arrivals of photons at the measurement devices for some clock cycles. In the third stage, computation is performed by measuring photons in a predetermined pattern, with the outcomes fed into a classical computer to determine the bases of subsequent measurements.

It can be seen that photonic hardware has distinct features that set it apart from solid-state hardware. Specifically, photonic qubits are continuously generated over time and consumed by measurements. The use of identical resource states simplifies hardware manufacture and enhances efficiency, but they are typically in a small size [29, 44] and the number of resources states generated in each clock cycle is limited by the number of RSGs. Moreover, photonic hardware features two types of connections: spatial and temporal, both of which support fusions but are subject to different constraints. For example, spatial routing may only occur between resource states generated by neighboring RSGs, while temporal routing may only occur between resource states generated by the same RSG within a limited delay time.
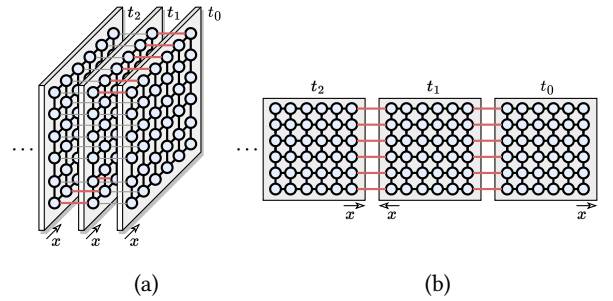

(a)   (b)

Figure 5: 3D structure of hardware connectivity (a) and its extendable space-time coupling graph (b). The physical layer t_1 in (b) is flipped in the horizontal direction so that the physical layers t_0, t_1 and t_2 and the their temporal connections in red form an extended physical layer. To keep the figure clear, other temporal connections are omitted in (b).

To capture these features, we formulate a hardware model abstraction called the *extendable space-time coupling graph*, as illustrated in Figure 5. Each node in the coupling graph represents a resource state generated by the RSG in the corresponding location, with resource states in different layers generated at different times. Each edge of the coupling graph represents a support for possible fusion operations. There are three levels of coupling, which we describe in detail below.

Coupling in the resource state The first level of coupling comes from entanglements of qubits in the same *resource state*. These entanglements are generated directly by the RSGs and do not require fusion operations. As a result, this level of coupling is implicit in Figure 5.

Coupling within physical layers The second level of coupling comes from the resource states generated within the same clock cycle, which together form a layer of qubits referred to as a *physical layer*. As shown in Figure 5, the nodes in the physical layer at t_0 (or t_1, t_2) are connected into a 2D lattice structure. Such connections within a clock cycle represent the spatial connections, which allows a resource state to conduct a fusion with resource states generated at the same time by its neighboring RSGs.

Coupling across physical layers The third level of coupling is that a resource state can make a fusion with another resource state generated in a different clock cycle by the same RSG, up to the limit of the delay time, as shown by the red and grey vertical lines in Figure 5(a). Note that we should avoid using too long-range temporal connections because photons suffer more from the loss error as they stay longer in the delay lines.

In the coupling graph, the physical layers are extendable by combining consecutive physical layers and keeping their temporal connections at boundary. For example, in Figure 5, the three physical layers (5(a)) generated at time t_0, t_1 and t_2 can form an *extended physical layer* by keeping their spatial connections and the temporal connections in red (5(b)), with physical layer t_1 being flipped in the x direction. Temporal connections other than the red ones are ignored in this extension and thus are not explicitly shown in Figure 5(b). This extendability makes the area of physical layers flexible, and can allow mapping of more global structures onto the physical layers.

Despite the similarity to the quantum hardware coupling graph [48] prevailing used for today's superconducting and ion trap hardware architectures, we emphasize on the differences between them as following.

1) Different levels of coupling are not independent, and actually their interplay could create some additional constraints. For example, suppose the resource states generated by RSGs are 3-qubit resource states, then although the fusion device allows each location on the physical layers to maximally connect to 4 spatial neighbors (up, down, left, right) and the corresponding locations on previous and future physical layers up to the limit of delay lines, only up to 3 of them can be activated.

2) The temporal connections are convertible to spatial connections in the extended physical layers. The 3D connectivity structure of the coupling graph can be flattened into a series of 2D extended physical layers along the time dimension, with each extended layer consisting of several consecutive physical layers. Within each extended physical layer, the temporal connections (red lines in Figure 5) are treated in the same way as spatial connections.

3.2 Overview of OneQ

As the first end-to-end compiler for MBQC, it is important to figure out a set of meaningful optimization goals. Our investigation on photonic one-way computing and realistic photonic quantum device development suggests the following two key optimization objectives. **1) Minimizing the physical depth**. The physical depth is defined as the number of physical layers consumed in the computation, which represents the time of executing the compiled program. **2) Reducing the number of fusions**. Fusions are often the most low-fidelity and costly operations incurred in such an MBQC photonic quantum computer.

In the rest of this subsection, we use a motivating example (shown in Figure 6) to give high-level ideas about the key challenges introduced in Section 1 and the insights of how they can be addressed by OneQ. We have attempted to maximize simplicity and ease of understanding, while possibly sacrificing some rigor. We often omit the dependency arrows and explicit measurement bases when they are not important for our optimization techniques, and they can always be derived from the graph state [46].

Challenge 1: Dynamic Computing Resources As resource states are generated dynamically in physical layers, a large number of qubits cannot be available simultaneously. In real-world quantum programs, graph states are typically too large (in terms of their number of nodes and edges) to be mapped onto a single or a few physical layers. Therefore, careful partition and scheduling schemes are needed to decompose large graph states into smaller components so that the graph state can be accommodated by the coordination of multiple physical layers. To minimize the delay time of photonic qubits and decrease their loss rates, dependent measurements can be scheduled according to their execution orders. However, this approach may compromise the compactness of graph state mapping onto the hardware by resulting in fragmented structures that lose the overall geometry of the graph state. In OneQ, this challenge is addressed by an approach that concurrently considers both the dependencies between measurements and the overall program geometry, allowing for a more efficient and effective allocation of resources. Section 4 gives detailed schemes of partition and scheduling.

Challenge 2: Lack of High-Degree Qubits High-degree nodes are a common occurrence in graph states, as qubits performing many two-qubit gates with other qubits (e.g. node G in Figure 6(a)) can result in high-degree qubit nodes in the corresponding graph state (e.g., node G in Figure 6(b)). However, such high-degree qubits may not be available in the resource states due to the limited interconnections among the photonic qubits they contain (e.g., qubits in the 3-qubit resource states in Figure 6(c) have a maximum degree of 2). This prevents a direct correspondence between the graph state nodes and the photonic qubits. In OneQ, those high-degree qubit nodes are synthesized by a proper strategy of fusions between low-degree qubits in resource states (e.g., node A to the shaded area in Figure 6(c), and node G to the area around G in the central part of Figure 6(c)). By matching with some basic fusion patterns, arbitrary high-degree input graph states (e.g., Figure 6(b)) can be synthesized to accommodate input adaptivity. Such a fusion strategy is agnostic to the routing constraints on the hardware, and aims to establish a viable fusion relation between resource states to synthesize the graph state eventually. The strategy can be abstracted to a *fusion graph* that indicate necessary fusions at the level of resource state. Section 5 gives detailed schemes for the generation of synthesis strategies and their fusion graphs.

Challenge 3: Mapping and Routing Constraints Due to the routing constraints, the irregular structure of fusions in Figure 6(b)
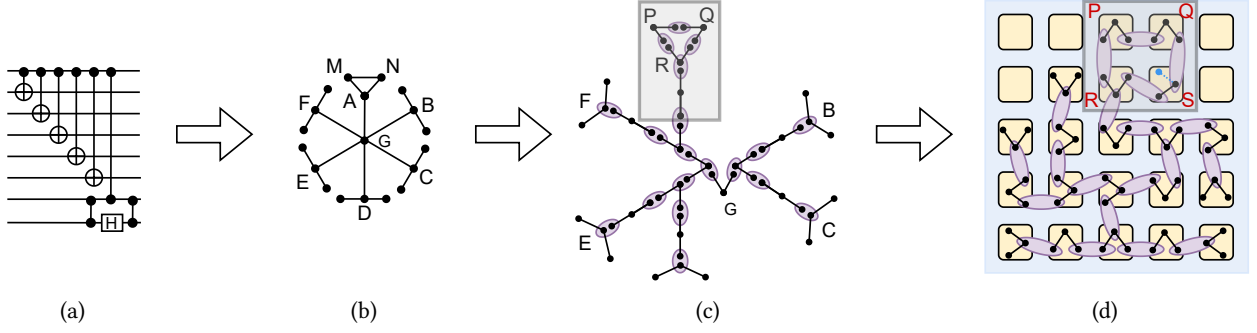
Figure 6: Compilation flow. (a) Quantum circuit. (b) Graph state. (c) Fusion graph generation. (d) Fusion mapping and routing.

may not be compatible with the hardware connectivity. In Figure 6(d), each yellow square represents a location of RGS, with the spatial routing allowing fusions between resource states from neighboring RGS's. It can be seen that the triangle in Figure 6(c) consisting of resource states P, Q and R (circled part in Figure 6(c)) cannot be mapped to the orthogonal grid directly because R can not be adjacent to both P and Q if P and Q are mapped to adjacent RSG locations. Such incompatibility exists widely in a general fusion graph, which prevents a direct mapping from the fusion graph to the underlying hardware topology. In OneQ this issue is resolved by extending some of the edges and winding them along the 2D lattice of individual or extended physical layers, which form paths of consecutive fusions. We refer to this procedure as fusion routing. For example, in Figure 6(d), P, Q and R can conduct fusions with each other with an auxiliary resource state S. In S, two qubits participate in the routing path RSQ, with the other qubit (in blue) removed by a Z-measurement. By maximizing the compactness of the mapping, we can minimize the overhead from extra fusions. Section 6 gives detailed searching schemes to map the edges onto orthogonal paths while minimizing the routing overhead.

Additional Challenge: Non-Planar Graph States The number of possible fusions on resource states is limited by the number of qubits they contain. Typically, for small resource states, each location in the coupling graph can be passed by at most one routing path. For example, in Figure 6(d), resource state S is passed by the routing path of edge QR, which destroys two of its qubits. This leaves only one qubit remaining, which is insufficient for use in another routing path. Therefore, the layout of the graph state cannot have edges intersecting each other unless the resource states are large enough to be splitted into multiple 2-qubit cluster states (e.g., as large as 5-qubit linear cluster state or 6-qubit ring-like cluster state). In other words, only *planar graphs*, i.e., graphs that can be embedded on a plane with no edges crossing each other, can be mapped to a single physical layer. In OneQ, this is addressed by enforcing a planarization process in all modules to prohibit the graph non-planarity.

4 Graph Partition and Scheduling

Scheduling of operations for MBQC differs from that for the circuit model in two ways. First, the dependency relations in MBQC can be quite different from those in the circuit model. For example, dependencies between measurements occur only in the presence of non-Clifford gates, while all measurements corresponding to

Clifford gates can be executed simultaneously. Second, the number of graph state nodes that can be accommodated by each physical layer is flexible, which is hard to predict beforehand since it depends on the strategies of graph synthesis and routing. Specifically, the synthesis of a node in the graph state may result in multiple nodes in the fusion graph, while the mapping of an edge in the fusion graph may require a routing path through multiple locations in the coupling graph.

To handle these distinct features, we partition the graph state into subgraphs in a way that respects the measurement dependency, and allow a dynamic scheduling for each subgraph to accommodate the flexibility in the resource demand. The graph partition enables the qubits measurable earlier to be scheduled onto earlier physical layers in a coarse grain, which reduces the wait time of qubits in the delay lines and enhances the program fidelity. The dynamic scheduling schedules each partition of the graph state onto a flexible number of physical layers, with the physical layers allocated dynamically until the partition is all mapped. This enables the search for a compact layout of the scheduled partition, which increases the efficiency of resource utilization and reduces the total number of physical layers required by the program.

The partition of the graph state respects the measurement dependency through an analysis of the executability order of the measurement operations. Due to the non-deterministic nature of quantum measurements, MBQC requires a classical feed-forward that induces dependencies between measurements. The partial order between measurements can be described by a causal flow [46], which is determined by two types of dependencies. Specifically, based on the measurement outcome of a particular qubit, the measurement angles of its neighboring qubits may be adjusted from α to $(-1)^s \alpha + t\pi$ where $s, t \in \{0, 1\}$, with the dependency on s called X-dependency and that on t called Z-dependency. Note that changing the angle from α to $\alpha + \pi$ only interchanges $|\pm_\alpha\rangle$ and $|\mp_\alpha\rangle$, which means the Z-dependency is equivalent to a re-interpretation of the measurement outcome of the affected qubit. Therefore the condition when a measurement becomes executable can be summarized as Lemma 1, with qubits executable at each time forming a *dependency layer*.

LEMMA 1. *A measurement on a qubit in the graph state is executable if all its X-dependent qubits are measured and all the Z-dependent qubits of all its X-dependent qubits are measured.*

This respect for measurement dependency is only in a coarse-grained manner. This means that a partition can contain multiple dependency layers, and dependency layers within the same partition do not have to be scheduled strictly according to their executability orders. The reason for this is two-fold. First, the presence of delay lines can allow the delay of qubits' arrival at the measurement devices for some time, making an exact match between the executability order and the physical layer order unnecessary. Second, allowing for this mismatch enables a preservation of the overall geometry structure among nearby dependency layers, which can be used to increase the potential compactness of the graph layout in the mapping process. Specifically, this coarse-grained manner can be achieved by first sorting the measurements according to their executability orders, and then forming each graph partition by including a number of consecutive dependency layers.

Partitioned subgraphs are then scheduled for fusion graph generation and layout search for the fusion graph in ascending order of their executability. The scheduling of these subgraphs is dynamic in two levels. First, for each partition, physical layers would be allocated dynamically for mapping and routing until all the nodes in the corresponding fusion graph are mapped to the hardware. Second, among partitions, there can be additional edges connecting nodes of fusion graphs for different partitions, which also need to be mapped to the hardware to form the whole graphs state. This can be achieved by dynamically allocating additional physical layers between the partitions, and routing on those physical layers until all cross-partition edges are mapped.

Graph Planarization To further respect the planarity constraint for resource states of small size, the planarity of the subgraphs can be used as an additional condition for graph partitioning. Specifically, in the process of grouping consecutive dependency layers into partitions in ascending order of their executability, a planarity check can be performed along the way. New dependency layers will not be included if either the limit number of dependency layers is exceeded or the accumulated subgraph is no longer a planar graph. If a single dependency layer is already non-planar, it can be decomposed into subgraphs by repeatedly finding the maximal planar subgraph G_i from its remaining graph G, where a maximal planar subgraph G_i is defined as a subgraph such that the addition of any edge $e \in G - G_i$ breaks the planarity of G_i. This planarization can ensure in advance that each partition scheduled for fusion graph generation and layout searching is a planar graph, avoiding unnecessary conflicts when the graph is large and complex.

5 Fusion Graph Generation

A graph state can be synthesized from small resource states via fusion by first synthesizing necessary components such as high-degree nodes and lines, then connecting them according to the graph geometry. In this section, we lay the foundation of synthesizing arbitrary graph states by defining a set of basic patterns. Then we demonstrate the process of graph synthesis from 3-qubit resource states and generalize it to more generic resource states.

Synthesis of arbitrary graph states can be realized by appropriate strategies based on some basic fusion patterns, as shown in Figure 7. First, the degree of a node V can be increased by a *degree increment* pattern, which fuses a leaf node (degree = 1) connecting to V with a node of degree > 1. For example, the degree of node V in Figure 7(a)
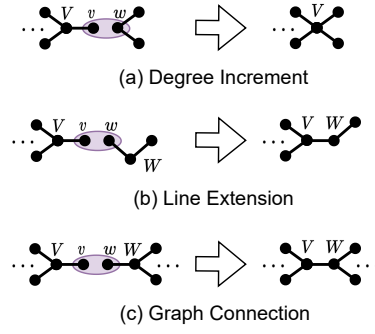

(a) Degree Increment

(b) Line Extension

(c) Graph Connection

Figure 7: Basic fusion patterns.

is increased by 1 by fusing node v with a 2-degree node w. Second, a line of nodes can be extended by a *line extension* pattern, which fuses a leaf node of the line with that of another line. For example, the 2-node line Vv in Figure 7(b) is extended to a 3-node line by fusing the leaf node v with the leaf node w. Third, two resource states can be connected while maintaining their structures (except the fused nodes) by a *graph connection* pattern, which fuses two leaf nodes from each of them respectively. For example, the two 4-node graphs in Figure 7(c) are connected by a fusion between node v and w, with the nodes V and W connected by an edge in the formed graph state and the remaining structures of them left unchanged.

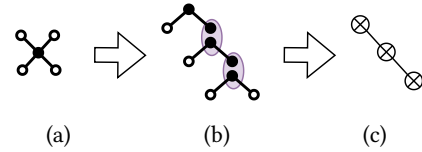(a)   (b)   (c)

Figure 8: Synthesize a high degree node in (a) by a basic fusion pattern in (b). Represent the fusion pattern by a fusion graph in (c), with each '⊗' node representing a resource state, each edge representing a fusion operation.

With these basic patterns, an arbitrary graph state can be synthesized from resource states as small as 3-qubit resource states. Specifically, high-degree nodes in the graph states can be synthesized by a repetitive application of the degree increment pattern until the required degree is satisfied, as shown in Figure 8(a)(b). The resulting fusion pattern can be represented by a *fusion graph* in Figure 8(c), with each node representing a resource state, and each edge representing a fusion operation. Similarly, lines can be synthesized by a repetitive application of the line extension pattern until the required length is satisfied. Then, the high degree nodes and lines can be connected via the graph connection pattern (Figure 7(c)). We demonstrate it with an example of synthesizing a graph in Figure 9(a). In Figure 9(b), we break down the graph into high degree nodes A, B, C, D, O and lines PQ, RS. Each high-degree node or each line is connected with some nodes in hollow dots, which represent its neighbors in Figure 9(a). Those nodes are referred to as *virtual nodes*. Note that multiple virtual nodes are
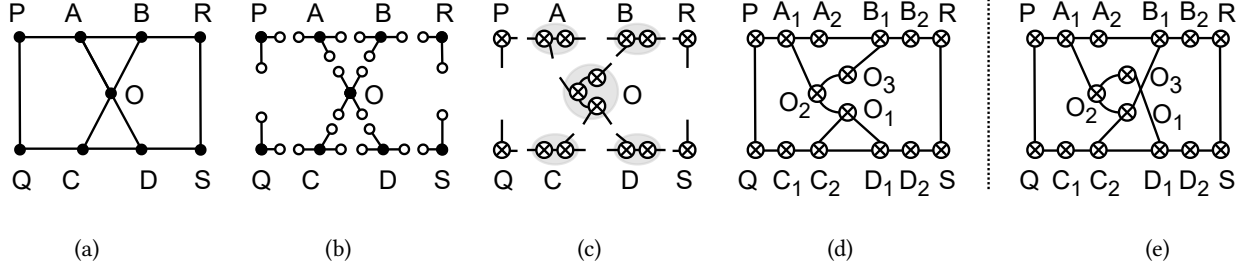
(a)　　　　　　(b)　　　　　　(c)　　　　　　(d)　　　　　　(e)

Figure 9: Fusion graph generation. (a) A planar embedding of the graph state geometry. (b) Split the edges. (c) Replace each high-degree node with a piece of fusion graph, with each '⊗' node representing a resource state. (d) Connect the pieces of fusion graphs while keeping the clockwise (counter-clockwise) edge orders in the planar embedding so as to obtain a planar fusion graph. (e) The planarity may be broken if not keeping the clockwise (counter-clockwise) edge orders.

allowed to represent the same node. We synthesize the high-degree nodes and lines with the basic patterns Figure 7(a)(b), pairing up the virtual nodes according to the original graph in Figure 9(a), and connect these components by applying the basic pattern Figure 7(c) on the paired virtual nodes.

For generic resource states, this synthesis process can be made applicable by a modification containing two steps. First, nodes of the fusion pattern in Figure 8(c) can be reduced by utilizing qubits of degree > 2. In particular, for resource states with max degree m, an n-degree node can be synthesized by $n//m+1$ resource states, where the extra ($n \bmod m$) qubits would be removed by Z-measurements. Therefore, the fusion graph in Figure 8(c) becomes a linear graph containing $n//m + 1$ nodes, instead of $n - 1$ nodes in the case of 3-qubit resource states. Second, edges in the fusion graph for 3-qubit GHZ states can be contracted by utilizing the connections between qubits within the resource states. This can be achieved by a pattern matching process that traverses the graph, searching for lines or cycles that match the intrinsic geometry of the resource states. During the synthesis process, qubits in resource states can be removed by Z-measurements when necessary. For example, a n-qubit ring-like resource state can be tailored to a $(n − 1)$-qubit linear resource state by removing one qubit, if linear structures, rather than rings, need to be synthesized.

Planarity Preservation The planarity condition imposed in the graph partition can be preserved in the process of fusion graph generation. In other words, if the original graph is planar, then the resulting fusion graph can also be planar. This can be achieved by first finding a planar embedding of the original graph, i.e., a way of drawing it on the plane with no crossing edges, and then keeping the clockwise (counterclockwise) orders among the edges when connecting the synthesized high-degree nodes. The search for the planar embedding can be efficiently done by existing tools such as Networkx [49]. For example, in the planar graph in Fig. 9(a), the 4-degree node O has neighbors A, B, D, C in the clockwise order. So we replace it with a fusion graph component consisting of 3 nodes (component O in the grey circle at the center of Fig. 9(c)), and connect it with fusion graph components of A, B, D, C in a clockwise manner (Fig. 9(d)). As a comparison, Fig. 9(e) shows a fusion graph that breaks planarity since the clockwise (counterclockwise) edge orders are not maintained.

6 Fusion Mapping and Routing

Finding the most compact layout of a graph on a grid is known to be an NP-hard problem [50], and it is particularly challenging in our case due to two additional features of the grid. First, each layer of grid has limited area because each physical layer of resource states is generated by limited number of RSGs. Second, the space-time coupling in the hardware has a 3D nature, which makes a direct search of mapping inefficient. In particular, each edge of a node can be mapped or routed toward not only different directions around the node but also any of the previous or subsequent layers up to the limit of delay time, which increases the search space and leads to longer search times.
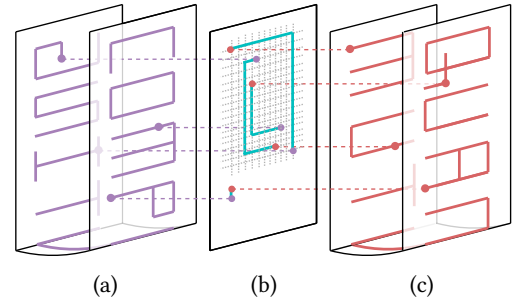

(a)　　　　(b)　　　　(c)

Figure 10: Mappings of 'QUANTUM' (red) and 'COMPUTING' (purple) connected through a shuffling layer (b) in between. Red dots on (c) represent the incomplete nodes whose edges are not all mapped yet, with the other ends of them being the purple dots on (a). Corresponding nodes are connected by a shuffling on the intermediate layer (green lines in (b)).

To address these challenges, we propose an algorithm consisting of an *in-layer mapping* and an *inter-layer shuffling*, which is applicable for grids of various geometry (triangular, orthogonal, etc.). It finds the 3D layout of the scheduled graph by finding a series of 2D compact layouts and connecting the them by a shuffling of nodes. Each 2D layout is found by a boundary-aware heuristic search restricted to a physical layer or extended physical layer. The *incomplete* nodes on each layer, whose edges are not all mapped due to the limited grid area are then connected by a node shuffling

on additional physical layer between the 2D layouts. For example, in Figure 10, the graph 'QUANTUM' (red) and 'COMPUTING' (purple) are mapped onto two extended physical layers in 10(c) and 10(a), respectively. Red dots on 10(c) represent the incomplete nodes whose edges are not all mapped yet, with the other ends of those edges being the incomplete nodes represented by the purple dots on 10(a). These incomplete nodes are connected by a shuffling on the intermediate layer 10(b), with the green lines being the routing paths between corresponding nodes.

In the in-layer mapping, each edge is mapped onto the physical layer or extended physical layer either directly or via routing. The routing is triggered in two scenarios. First, it can map the edges between existing nodes in the layout, thus allowing the fusion between non-neighboring nodes and accommodating the irregularity in the structure of the scheduled graph. Second, it is used to reduce the blockage between mapped nodes and future nodes, thus increasing the number of edges that can be mapped to the layer and maximizing compactness of the layout. A node is defined as *blocked* if the number of its remaining unmapped edges r exceeds the number of its adjacent available positions on the grid s, with the case of $s > 0$ called *partially blocked* and the case of $s = 0$ called *totally blocked*. When a node is partially blocked by other mapped nodes, we can route the node to a position that has enough available degrees. When the direct mapping of an edge result in a total blockage for some other nodes in the map, we can route the node to a broader area before the mapping, such that it leaves enough degrees for the other nodes.
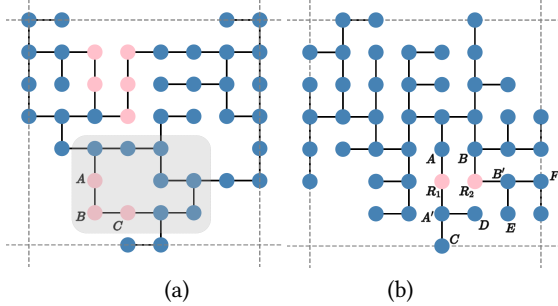

(a)   (b)

Figure 11: (a) Mapping of fusion graph for 8-qubit BV with secret string '11111111'. (b) Mapping of fusion graph for 3-qubit QFT. Blue and green dots correspond to the nodes '⊗' existing in the fusion graph, with the green ones being the incomplete nodes whose edges are not all mapped yet. Pink dots represent the auxiliary resource states used for routing.

This can be more clearly demonstrated with two layout examples. In Figure 11(a), the routing path ABC, represented by pink nodes, is used to connect the existing nodes and form the cyclic structure in the shaded area. In Figure 11(b), routing was triggered for twice. First, node A' is routed from R_1 by one step to avoid the total blockage for node B, because if node A' is directly mapped to the location R_1, one of its edges $A'C$ and $A'D$ would have to take location R_2, which is the only remaining location around B. Second, node B' is routed by one step to address its partial blockage by $A'D$,

because while node B' can be directly mapped to the location R_2, the only one remaining location around it would be insufficient for mapping its two future edges $B'E$ and $B'F$. Note that in real cases the length of routing paths should be ≥ 2.

The heuristic search algorithm can be stated as below. We traverse the edges in a cycle-prioritized breadth-first order, giving priority to edges involved in cycles over those in trees, because tree edges are more flexible for mapping. We choose to map each edge either directly or via routing according to the scenarios above. After each new edge is mapped, the layout is evaluated by the heuristic cost function

$$
\begin{aligned}
H = \ & \text{occupied\_area} \\
& + \text{\#partially\_blocked\_nodes} \\
& + \alpha \cdot \text{\#totally\_blocked\_nodes}
\end{aligned}
$$

where occupied_area refers to the area of the smallest rectangle that can enclose the mapped edges. α should be larger than 1 as a total blockage is more harmful. It can be typically set as the maximum degree of each physical layer. The layout with the lowest cost is then selected as the best candidate and used in the search for future edges.

In the inter-layer shuffling, incomplete nodes in different 2D layouts are connected via routing on the physical layers allocated between them. This shuffling can be achieved by first pairing up the incomplete nodes, sorting the node pairs according to their distances, and then finding the shortest routing paths to connect the node pairs in ascending order of the distances. Specifically, if a single physical layer is not enough to accommodate all the routing paths, more physical layers can be allocated dynamically until all the node pairs are connected. The inter-layer shuffling can be used to support the subgraph connection need arising in two circumstances. First, as the graph partition process partitions the whole graph state into subgraphs, the fusion graphs of different subgraphs need to be connected to form the whole graph state. Second, the mapping of each partition may generate multiple 2D layouts, as some nodes may be inevitably blocked due to the limited area of physical layers and the complexity of the graph geometry. While positions of incomplete nodes in the previous layers are taken into account in the mapping of subsequent layers to increase their proximity, those 2D layouts may still need to be connected by the inter-layer shuffling if not all conflicts can be resolved within the in-layer mapping.

Planarity-Aware Search When the given fusion graph is planar, the heuristic search for in-layer mapping can be made planarity-aware to maximize the number of edges accommodated by each physical layer. Specifically, we can first find a planar embedding of the fusion graph, and make the mapping of each edge follow the planar embedding, which can be achieved by forcing the mapped edge to leave enough degrees for its clockwise or counterclockwise neighboring edges connected to the same node. This planarity-awareness naturally prevents routing paths from crossing each other and reduces the demand for inter-layer shuffling. This approach is more effective when the area of physical layers is large enough, because otherwise the edges would be blocked by the limited area anyway. This area can be increased by extension of physical layers, as shown in Figure 5(b).

7 Evaluation

7.1 Experiment Setup

Metric As discussed in Section 3.2, the first metric we consider is the physical depth, i.e., the number of physical layers consumed in the execution of the program. The second metric is the number of fusion operations performed in the execution of the program, which is denoted as '# fusion'. A better compiler should compile a quantum program into a smaller depth which indicates a shorter execution time and less consumption of resources, and a smaller '# fusion' which indicates less overhead and being less error-prone. For comparison with the baseline, we define an improvement factor of physical depth as the ratio of the depth in the baseline to the depth in OneQ, and an improvement factor of '# fusion' as the ratio of the number of fusions consumed in the baseline to the that consumed in OneQ.

Baseline Our optimized baseline is based on the basic MBQC interpreter introduced in Section 2 but with two preprocessing steps. The first step is synthesizing a sufficiently large 3D cluster state by fusions from small resource states generated by the RSGs. The sufficient size of each 2D layer of the cluster state is referred to as *cluster area*, while the number of RSGs required to form a cluster state of that size is referred to as *physical area*. The second step is finding a layout for the circuit so that measurement patterns of all gates in the circuit can be joined in a way shown as Figure 4.

For the first step, instead of relying on any specific synthesis strategy, we adopt a lower bound of the physical area, which indicates the least number of required resource states when ignoring the spatial constraints for fusion routing. For the second step, to ensure an efficient implementation of a two-qubit gate with MBQC, it is necessary to place the strips of the involved qubits close to each other in the cluster state, similar to that in the circuit model with solid-state-qubit quantum computing. As a result, we utilize the qubit mapping and routing functions of Qiskit [21] to address the issues related to far-apart 2-qubit gates prior to mapping the circuit onto the cluster state. Specifically, this is achieved by using a 2D coupling graph that shares the same structure with each 2D layer of the cluster state as the hardware coupling graph to Qiskit.

Benchmark programs We select Quantum Fourier transform (QFT), quantum approximate optimization algorithm (QAOA), Ripple-Carry Adder (RCA) [51] and Bernstein-Vazirani (BV) algorithm as our benchmarks, which include both building blocks of quantum programs (QFT and RCA) and application driven programs targeting at solving real-world problems (QAOA and BV). For QAOA, we choose the graph maxcut problem on randomly generated graphs. Specifically, the graphs are generated by randomly selecting half of its all possible edges. For BV, we select the secret strings randomly, with approximately half of the digits being 0 and half being 1. In table 1, we list the number of qubits and the number of gates for each benchmark, as well as the cluster area and physical area required by the baseline approach. For each benchmark, our framework is evaluated on the same physical area with the baseline to make them more comparable.

7.2 Experiment Result

We first show the results of the baseline and OneQ for 3-qubit resource states in Table 2, as the number of qubits increases for each benchmark. It can be seen that OneQ outperforms the baseline

Table 1: Benchmark programs.

Name	#qubit	cluster area	physical area
Quantum Fourier Transform (QFT)	16	7x7	16x16
	25	9x9	21x21
	36	11x11	25x25
Quantum Approximate Optimization Alg (QAOA)	16	7x7	16x16
	25	9x9	21x21
	36	11x11	25x25
Ripple-Carry Adder (RCA)	16	7x7	16x16
	25	9x9	21x21
	36	11x11	25x25
Bernstein Vazirani (BV)	16	7x7	16x16
	25	9x9	21x21
	100	19x19	43x43

by orders of magnitude in both physical depth and the number of fusions. As the number of qubits increases, this improvement of performance stays stable or slightly increases.
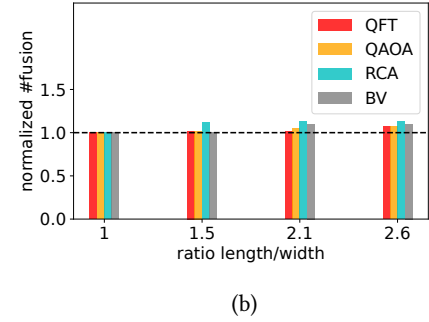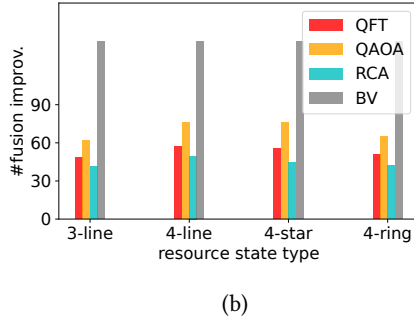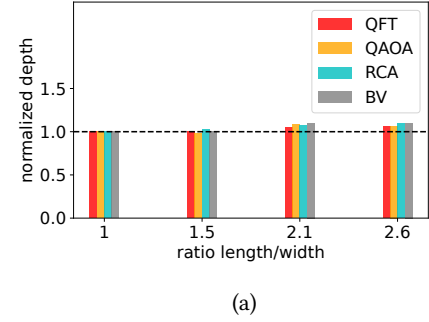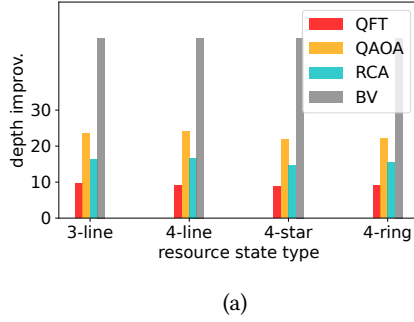
Among the benchmarks, OneQ has the most significant improvement for BV. This is because the graph state of BV is acyclic and planar, making it easier the heuristic search in OneQ to find a compact layout for the graph and map it to only a few physical layers. In contrast, the graph states of the QFT, QAOA and RCA contain a lot of short-range and long-range cycles, which makes the structure more complex and increases the demand for routing. However, for these benchmarks, OneQ still achieves a reduction on the physical depth by a factor of 15 on average (geomean), and a reduction on the number of fusions by a factor of 47 on average (geomean).

General resource states To achieve greater generality, our optimization modules are designed to be extendable to a wide range of resource states. This is made possible by accommodating flexible fusion strategies for synthesizing graph states and representing each strategy with a fusion graph. Figure 12 shows the results when the resource states are 3-qubit line-shaped graph state, 4-qubit line-shaped, star-shaped and ring-shaped graphs states, respectively. The improvements in physical depth and the number of fusions are shown in (a) and (b), respectively. It can be seen that OneQ achieves similar levels of improvement in performance for these various resource states.

Flexible coupling structure While the results in Table 2 are on physical layers of $N \times N$ square coupling structure, OneQ is applicable to more general coupling structures. Figure 13 shows the physical depth (13(a)) and the number of fusions (13(b)) when the ratio of each physical layer is 16x16 (ratio = 1), 20x13 (ratio = 1.5), 23x11 (ratio = 2.1) and 26x10 (ratio = 2.6) respectively. For comparison, the results are normalized by those on the square physical layer. It can be seen that OneQ achieves similar levels of performance on these various shapes of physical layers. Moreover, the area of physical layers is adjustable by regarding multiple consecutive physical layers as an extended physical layer, which can be

Table 2: The results of OneQ and its relative performance to the baseline.

Name-#qubits	Baseline Depth	Our Depth	Improv. Factor	Baseline #Fusions	Our #Fusions	Improv. Factor
QFT-16	787	83	9	201,472	8,167	25
QFT-25	1,518	162	9	669,438	26,921	25
QFT-36	2,712	324	8	1,695,000	66,830	25
QAOA-16	595	29	20	152,320	2,578	59
QAOA-25	1,287	63	20	567,567	8,343	68
QAOA-36	2,648	122	22	1,655,000	21,302	78
RCA-16	734	46	16	187,904	4,568	41
RCA-25	1,273	65	20	561,393	8,915	63
RCA-36	1,934	85	23	1,208,750	14,115	86
BV-16	94	1	92	24,064	63	382
BV-25	181	1	181	79,821	114	700
BV-100	787	4	197	1,455,163	644	2,260

(a)

(b)

Figure 12: Improvement factors of physical depth (a) and # fusions (b) of 16-qubit QFT, QAOA, RAC and BV for different basic resource states.

(a)

(b)

Figure 13: Normalized physical depth (a) and # fusions (b) of 16-qubit QFT, QAOA, RCA and BV on different shapes of physical layers. Results on rectangular physical layers (ratio > 1) are normalized by those on square physical layers (ratio = 1).

used to accommodate more global structure of the graph. As a demonstration, Figure 14 shows a slice of mapping generated by OneQ for a 16-qubit QFT program. The whole rectangular 13 × 39 extended physical layer is composed of 3 layers of 13 × 13 grid. The first physical layer ranges from column 1 to column 13, the second ranges from column 14 to column 26, and the third from column 27

to column 39 respectively. In the figure, blue and green dots correspond to the nodes '⊗' existing in the fusion graph, with the green ones representing the incomplete nodes, which means that some of edges connected to them have not been mapped onto the grid.
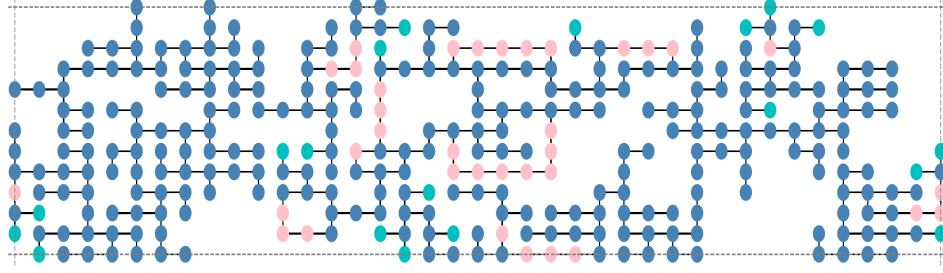
Figure 14: Mapping of the fusion graph of a 16-qubit QFT program with a more global optimization by considering an extended physical layer consisting of 3 successive physical layers of size 13×13. Blue and green dots correspond to the nodes '⊗' existing in the fusion graph, with the green ones being the incomplete nodes whose edges are not all mapped yet. Pink dots represent the auxiliary resource states used for routing.

Pink dots represent the auxiliary resource states used for routing. In principle, the optimization techniques in OneQ is also applicable when the coupling structure between RSGs are not orthogonal (e.g., triangular, hexagonal) since none of our optimization modules has explicit dependency on a specific coupling architecture.
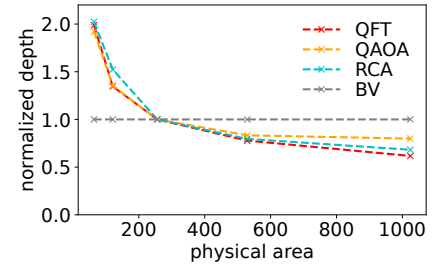
Effect of physical area In contrast to the fixed size of physical layers required by the baseline approach, OneQ does not impose strict constraints on the size of physical layers, allowing programs to be compiled onto hardware of different sizes. Specifically, the physical depth can be decreased by allowing longer routing paths on larger physical layers, with a cost of more fusions. Figure 15 shows the physical depth and the number of fusions when the programs are compiled onto different sizes of physical layers. For comparison, the results are normalized by those on the physical area required by the baseline approach, which is 16x16 when the number of qubits is 16. It can be seen that when the physical area increases, the physical depth initially decreases rapidly, but eventually reaches a plateau when the physical area becomes sufficiently large. On the other hand, the number of fusions shows a reverse trend, increasing as the physical area increases. Note that if physical layers are larger than necessary, they can be truncated by restricting compilation to a portion of the physical layers.
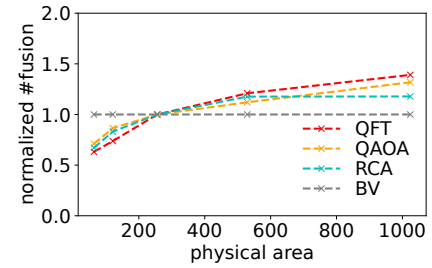
8 Conclusion

In this work, we provide in-depth analysis and discussion of the unique challenges for photonic one-way computing at both programming and hardware levels. We build the first end-to-end compilation framework for optimizing the mapping of any quantum programs onto photonic devices supported by our hardware abstract model. With this being said, many of the optimization problems here are NP-hard problems, and thus we believe there is still significant potential for fully exploring the entire optimization space. As the first work in this direction, we hope our work could attract more effort from the computer architecture and compiler community to explore the advantages of photonic quantum architectures and overcome the unique challenges.

Acknowledgments

(a)

(b)

Figure 15: Normalized physical depth (a) and # fusions (b) of 16-qubit QFT, QAOA, RAC and BV for different physical areas. Results on different physical areas are normalized by those on the same physical area as required by the baseline approach.

References

[1] Peter W Shor. Polynomial-time algorithms for prime factorization and discrete logarithms on a quantum computer. *SIAM review*, 41(2):303–332, 1999.

[2] Lov K Grover. A fast quantum mechanical algorithm for database search. In *Proceedings of the twenty-eighth annual ACM symposium on Theory of computing*, pages 212–219, 1996.

[3] Yudong Cao, Jonathan Romero, Jonathan P. Olson, Matthias Degroote, Peter D. Johnson, Mária Kieferová, Ian D. Kivlichan, Tim Menke, Borja Peropadre, Nicolas P.D. Sawaya, Sukin Sim, Libor Veis, and Alán Aspuru-Guzik. Quantum Chemistry in the Age of Quantum Computing. *Chemical Reviews*, 119:10856–10915, 2019.

[4] Sam McArdle, Suguru Endo, Alán Aspuru-Guzik, Simon C Benjamin, and Xiao Yuan. Quantum computational chemistry. *Reviews of Modern Physics*, 92(1):015003,

2020.

[5] Michel H Devoret and Robert J Schoelkopf. Superconducting circuits for quantum information: an outlook. *Science*, 339(6124):1169–1174, 2013.

[6] Colin D Bruzewicz, John Chiaverini, Robert McConnell, and Jeremy M Sage. Trapped-ion quantum computing: Progress and challenges. *Applied Physics Reviews*, 6(2):021314, 2019.

[7] Mark Saffman. Quantum computing with atomic qubits and rydberg interactions: progress and challenges. *Journal of Physics B: Atomic, Molecular and Optical Physics*, 49(20):202001, 2016.

[8] Pieter Kok, William J Munro, Kae Nemoto, Timothy C Ralph, Jonathan P Dowling, and Gerard J Milburn. Linear optical quantum computing with photonic qubits. *Reviews of modern physics*, 79(1):135, 2007.

[9] Shuntaro Takeda and Akira Furusawa. Toward large-scale fault-tolerant universal photonic quantum computing. *APL Photonics*, 4(6):060902, 2019.

[10] Mihir Pant, Don Towsley, Dirk Englund, and Saikat Guha. Percolation thresholds for photonic quantum computing. *Nature communications*, 10(1):1–11, 2019.

[11] Jeremy L. O'Brien, Akira Furusawa, and Jelena Vučković. Photonic quantum technologies. *Nature Photonics*, 3(12):687, 2009.

[12] S. Bogdanov, M. Y. Shalaginov, A. Boltasseva, and V. M. Shalaev. Material platforms for integrated quantum photonics. *Opt. Mater. Express*, 7(1):111–132, Jan 2017.

[13] Mikkel V Larsen, Xueshi Guo, Casper R Breum, Jonas S Neergaard-Nielsen, and Ulrik L Andersen. Deterministic multi-mode gates on a scalable photonic quantum computing platform. *Nature Physics*, 17(9):1018–1023, 2021.

[14] Jianwei Wang, Fabio Sciarrino, Anthony Laing, and Mark G Thompson. Integrated photonic quantum technologies. *Nature Photonics*, 14(5):273–284, 2020.

[15] Lars S. Madsen, Fabian Laudenbach, Mohsen Falamarzi. Askarani, Fabien Rortais, Trevor Vincent, Jacob F. F. Bulmer, Filippo M. Miatto, Leonhard Neuhaus, Lukas G. Helt, Matthew J. Collins, Adriana E. Lita, Thomas Gerrits, Sae Woo Nam, Varun D. Vaidya, Matteo Menotti, Ish Dhand, Zachary Vernon, Nicolás Quesada, and Jonathan Lavoie. Quantum computational advantage with a programmable photonic processor. *Nature*, 606(7912):75–81, Jun 2022.

[16] Han-Sen Zhong, Hui Wang, Yu-Hao Deng, Ming-Cheng Chen, Li-Chao Peng, Yi-Han Luo, Jian Qin, Dian Wu, Xing Ding, Yi Hu, Peng Hu, Xiao-Yan Yang, Wei-Jun Zhang, Hao Li, Yuxuan Li, Xiao Jiang, Lin Gan, Guangwen Yang, Lixing You, Zhen Wang, Li Li, Nai-Le Liu, Chao-Yang Lu, and Jian-Wei Pan. Quantum computational advantage using photons. *Science*, 370(6523):1460–1463, 2020.

[17] Han-Sen Zhong, Yu-Hao Deng, Jian Qin, Hui Wang, Ming-Cheng Chen, Li-Chao Peng, Yi-Han Luo, Dian Wu, Si-Qiu Gong, Hao Su, Yi Hu, Peng Hu, Xiao-Yan Yang, Wei-Jun Zhang, Hao Li, Yuxuan Li, Xiao Jiang, Lin Gan, Guangwen Yang, Lixing You, Zhen Wang, Li Li, Nai-Le Liu, Jelmer J. Renema, Chao-Yang Lu, and Jian-Wei Pan. Phase-programmable gaussian boson sampling using stimulated squeezed light. *Phys. Rev. Lett.*, 127:180502, Oct 2021.

[18] Sara Bartolucci, Patrick Birchall, Hector Bombin, Hugo Cable, Chris Dawson, Mercedes Gimeno-Segovia, Eric Johnston, Konrad Kieling, Naomi Nickerson, Mihir Pant, Fernando Pastawski, Terry Rudolph, and Chris Sparrow. Fusion-based quantum computation. *arXiv preprint arXiv:2101.09310*, 2021.

[19] Hector Bombin, Isaac H Kim, Daniel Litinski, Naomi Nickerson, Mihir Pant, Fernando Pastawski, Sam Roberts, and Terry Rudolph. Interleaving: Modular architectures for fault-tolerant photonic quantum computing. *arXiv preprint arXiv:2103.08612*, 2021.

[20] Sara Bartolucci, Patrick Birchall, Damien Bonneau, Hugo Cable, Mercedes Gimeno-Segovia, Konrad Kieling, Naomi Nickerson, Terry Rudolph, and Chris Sparrow. Switch networks for photonic fusion-based quantum computing. *arXiv preprint arXiv:2109.13760*, 2021.

[21] MD SAJID ANIS, Héctor Abraham, AduOffei, Rochisha Agarwal, Gabriele Agliardi, Merav Aharoni, Ismail Yunus Akhalwaya, Gadi Aleksandrowicz, Thomas Alexander, Matthew Amy, Sashwat Anagolum, Eli Arbel, Abraham Asfaw, Anish Athalye, Artur Avkhadiev, Carlos Azaustre, PRATHAMESH BHOLE, Abhik Banerjee, Santanu Banerjee, Will Bang, Aman Bansal, Panagiotis Barkoutsos, Ashish Barnawal, George Barron, George S. Barron, Luciano Bello, Yael Ben-Haim, M. Chandler Bennett, Daniel Bevenius, Dhruv Bhatnagar, Arjun Bhobe, Paolo Bianchini, Lev S. Bishop, Carsten Blank, Sorin Bolos, Soham Bopardikar, Samuel Bosch, Sebastian Brandhofer, Brandon, Sergey Bravyi, Nick Bronn, Bryce-Fuller, David Bucher, Artemiy Burov, Fran Cabrera, Padraic Calpin, Lauren Capelluto, Jorge Carballo, Ginés Carrascal, Adam Carriker, Ivan Carvalho, Adrian Chen, Chun-Fu Chen, Edward Chen, Jielun (Chris) Chen, Richard Chen, Franck Chevallier, Kartik Chinda, Rathish Cholarajan, Jerry M. Chow, Spencer Churchill, CisterMoke, Christian Claus, Christian Clauss, Caleb Clothier, Romilly Cocking, Ryan Cocuzzo, Jordan Connor, Filipe Correa, Abigail J. Cross, Andrew W. Cross, Simon Cross, Juan Cruz-Benito, Chris Culver, Antonio D. Córcoles-Gonzales, Navaneeth D, Sean Dague, Tareq El Dandachi, Animesh N Dangwal, Jonathan Daniel, Marcus Daniels, Matthieu Dartiailh, Abdón Rodríguez Davila, Faisal Debouni, Anton Dekusar, Amol Deshmukh, Mohit Deshpande, Delton Ding, Jun Doi, Eli M. Dow, Eric Drechsler, Eugene Dumitrescu, Karel Dumon, Ivan Duran, Kareem EL-Safty, Eric Eastman, Grant Eberle, Amir Ebrahimi, Pieter Eendebak, Daniel Egger, ElePT, Emilio, Alberto Espiricueta, Mark Everitt, Davide Facoetti, Farida, Paco Martín Fernández, Samuele Ferracin, Davide Ferrari, Axel Hernández Ferrera, Romain Fouilland, Albert Frisch, Andreas Fuhrer, Bryce Fuller, MELVIN GEORGE, Julien Gacon, Borja Godoy Gago, Claudio Gambella, Jay M. Gambetta, Adhisha Gammanpila, Luis Garcia, Tanya Garg, Shelly Garion, James R. Garrison, Tim Gates, Leron Gil, Austin Gilliam, Aditya Giridharan, Juan Gomez-Mosquera, Gonzalo, Salvador de la Puente González, Jesse Gorzinski, Ian Gould, Donny Greenberg, Dmitry Grinko, Wen Guan, Dani Guijo, John A. Gunnels, Harshit Gupta, Naman Gupta, Jakob M. Günther, Mikael Haglund, Isabel Haide, Ikko Hamamura, Omar Costa Hamido, Frank Harkins, Kevin Hartman, Areeq Hasan, Vojtech Havlicek, Joe Hellmers, Łukasz Herok, Stefan Hillmich, Hiroshi Horii, Connor Howington, Shaohan Hu, Wei Hu, Junye Huang, Rolf Huisman, Haruki Imai, Takashi Imamichi, Kazuaki Ishizaki, Ishwor, Raban Iten, Toshinari Itoko, Alexander Ivrii, Ali Javadi, Ali Javadi-Abhari, Wahaj Javed, Qian Jianhua, Madhav Jivrajani, Kiran Johns, Scott Johnstun, Jonathan-Shoemaker, JosDenmark, JoshDumo, John Judge, Tal Kachmann, Akshay Kale, Naoki Kanazawa, Jessica Kane, Kang-Bae, Annanay Kapila, Anton Karazeev, Paul Kassebaum, Josh Kelso, Scott Kelso, Vismai Khanderao, Spencer King, Yuri Kobayashi, Kovi11Day, Arseny Kovyrshin, Rajiv Krishnakumar, Vivek Krishnan, Kevin Krsulich, Prasad Kumar, Gawel Kus, Ryan LaRose, Enrique Lacal, Raphaël Lambert, Haggai Landa, John Lapeyre, Joe Latone, Scott Lawrence, Christina Lee, Gushu Li, Jake Lishman, Dennis Liu, Peng Liu, Abhishek K M, Liam Madden, Yunho Maeng, Saurav Maheshkar, Kahan Majmudar, Aleksei Malyshev, Mohamed El Mandouh, Joshua Manela, Manjula, Jakub Marecek, Manoel Marques, Kunal Marwaha, Dmitri Maslov, Paweł Maszota, Dolph Mathews, Atsushi Matsuo, Farai Mazhandu, Doug McClure, Maureen McElaney, Cameron McGarry, David McKay, Dan McPherson, Srujan Meesala, Dekel Meirom, Corey Mendell, Thomas Metcalfe, Martin Mevissen, Andrew Meyer, Antonio Mezzacapo, Rohit Midha, Daniel Miller, Zlatko Minev, Abby Mitchell, Nikolaj Moll, Alejandro Montanez, Gabriel Monteiro, Michael Duane Mooring, Renier Morales, Niall Moran, David Morcuende, Seif Mostafa, Mario Motta, Romain Moyard, Prakash Murali, Jan Müggenburg, Tristan NEMOZ, David Nadlinger, Ken Nakanishi, Giacomo Nannicini, Paul Nation, Edwin Navarro, Yehuda Naveh, Scott Wyman Neagle, Patrick Neuweiler, Aziz Ngoueya, Johan Nicander, Nick-Singstock, Pradeep Niroula, Hassi Norlen, NuoWenLei, Lee James O'Riordan, Oluwatobi Ogunbayo, Pauline Ollitrault, Tamiya Onodera, Raul Otaolea, Steven Oud, Dan Padilha, Hanhee Paik, Soham Pal, Yuchen Pang, Ashish Panigrahi, Vincent R. Pascuzzi, Simone Perriello, Eric Peterson, Anna Phan, Kuba Pilch, Francesco Piro, Marco Pistoia, Christophe Piveteau, Julia Plewa, Pierre Pocreau, Alejandro Pozas-Kerstjens, Rafał Pracht, Milos Prokop, Viktor Prutyanov, Sumit Puri, Daniel Puzzuoli, Jesús Pérez, Quant02, Quintiii, Rafey Iqbal Rahman, Arun Raja, Roshan Rajeev, Isha Rajput, Nipun Ramagiri, Anirudh Rao, Rudy Raymond, Oliver Reardon-Smith, Rafael Martín-Cuevas Redondo, Max Reuter, Julia Rice, Matt Riedemann, Rietesh, Drew Risinger, Marcello La Rocca, Diego M. Rodríguez, RohithKarur, Ben Rosand, Max Rossmannek, Mingi Ryu, Tharrmashastha SAPV, Nahum Rosa Cruz Sa, Arijit Saha, Abdullah Ash-Saki, Sankalp Sanand, Martin Sandberg, Hirmay Sandesara, Ritvik Sapra, Hayk Sargsyan, Aniruddha Sarkar, Ninad Sathaye, Bruno Schmitt, Chris Schnabel, Zachary Schoenfeld, Travis L. Scholten, Eddie Schoute, Mark Schulterbrandt, Joachim Schwarm, James Seaward, Sergi, Ismael Faro Sertage, Kanav Setia, Freya Shah, Nathan Shammah, Rohan Sharma, Yunong Shi, Jonathan Shoemaker, Adenilton Silva, Andrea Simonetto, Deeksha Singh, Divyanshu Singh, Parmeet Singh, Phattharaporn Singkanipa, Yukio Siraichi, Siri, Jesús Sistos, Iskandar Sitdikov, Seyon Sivarajah, Magnus Berg Sletfjerding, John A. Smolin, Mathias Soeken, Igor Olegovich Sokolov, Igor Sokolov, Vicente P. Soloviev, SooluThomas, Starfish, Dominik Steenken, Matt Stypulkoski, Adrien Suau, Shaojun Sun, Kevin J. Sung, Makoto Suwama, Oskar Słowik, Hitomi Takahashi, Tanvesh Takawale, Ivano Tavernelli, Charles Taylor, Pete Taylour, Soolu Thomas, Kevin Tian, Mathieu Tillet, Maddy Tod, Miroslav Tomasik, Caroline Tornow, Enrique de la Torre, Juan Luis Sánchez Toural, Kenso Trabing, Matthew Treinish, Dimitar Trenev, TrishaPe, Felix Truger, Georgios Tsilimigkounakis, Davindra Tulsi, Wes Turner, Yotam Vaknin, Carmen Recio Valcarce, Francois Varchon, Adish Vartak, Almudena Carrera Vazquez, Prajjwal Vijaywargiya, Victor Villar, Bhargav Vishnu, Desiree Vogt-Lee, Christophe Vuillot, James Weaver, Johannes Weidenfeller, Rafal Wieczorek, Jonathan A. Wildstrom, Jessica Wilson, Erick Winston, WinterSoldier, Jack J. Woehr, Stefan Woerner, Ryan Woo, Christopher J. Wood, Ryan Wood, Steve Wood, James Wootton, Matt Wright, Lucy Xing, Jintao YU, Bo Yang, Unchun Yang, Daniyar Yeralin, Ryota Yonekura, David Yonge-Mallo, Ryuhei Yoshida, Richard Young, Jessie Yu, Lebin Yu, Christopher Zachow, Laura Zdanski, Helena Zhang, Iulia Zidaru, and Christa Zoufal. Qiskit: An open-source framework for quantum computing, 2021.

[22] Seyon Sivarajah, Silas Dilkes, Alexander Cowtan, Will Simmons, Alec Edgington, and Ross Duncan. t| ket>: a retargetable compiler for nisq devices. *Quantum Science and Technology*, 6(1):014003, 2020.

[23] Robert Raussendorf. Measurement-based quantum computation with cluster states. *International Journal of Quantum Information*, 7(06):1053–1203, 2009.

[24] Nathan Killoran, Josh Izaac, Nicolás Quesada, Ville Bergholm, Matthew Amy, and Christian Weedbrook. Strawberry fields: A software platform for photonic quantum computing. *Quantum*, 3:129, 2019.

[25] Craig S Hamilton, Regina Kruse, Linda Sansoni, Sonja Barkhofen, Christine Silberhorn, and Igor Jex. Gaussian boson sampling. *Physical review letters*, 119(17):170501, 2017.

[26] Robert Raussendorf, Daniel E Browne, and Hans J Briegel. Measurement-based quantum computation on cluster states. *Physical review A*, 68(2):022312, 2003.

[27] Hans J Briegel, David E Browne, Wolfgang Dür, Robert Raussendorf, and Maarten Van den Nest. Measurement-based quantum computation. *Nature Physics*, 5(1):19–26, 2009.

[28] Maarten Van den Nest, Akimasa Miyake, Wolfgang Dür, and Hans J Briegel. Universal resources for measurement-based quantum computation. *Physical review letters*, 97(15):150504, 2006.

[29] Mercedes Gimeno-Segovia, Pete Shadbolt, Dan E Browne, and Terry Rudolph. From three-photon ghz states to universal ballistic quantum computation. 2015.

[30] Hans J Briegel and Robert Raussendorf. A one-way quantum computer. *Physical Review Letters*, 86(22), 2003.

[31] Michael A Nielsen. Optical quantum computation using cluster states. *Physical review letters*, 93(4):040503, 2004.

[32] Sébastien Tanzilli, Anthony Martin, Florian Kaiser, Marc P De Micheli, Olivier Alibart, and Daniel B Ostrowsky. On the genesis and evolution of integrated quantum optics. *Laser & Photonics Reviews*, 6(1):115–143, 2012.

[33] Philip Walther, Kevin J Resch, Terry Rudolph, Emmanuel Schenck, Harald Weinfurter, Vlatko Vedral, Markus Aspelmeyer, and Anton Zeilinger. Experimental one-way quantum computing. *Nature*, 434(7030):169–176, 2005.

[34] Giuseppe Vallone, Gaia Donati, Natalia Bruno, Andrea Chiuri, and Paolo Mataloni. Experimental realization of the deutsch-jozsa algorithm with a six-qubit cluster state. *Physical Review A*, 81(5):050302, 2010.

[35] Mark S Tame, Bryn A Bell, Carlo Di Franco, William J Wadsworth, and John G Rarity. Experimental realization of a one-way quantum computer algorithm solving simon's problem. *Physical Review Letters*, 113(20):200501, 2014.

[36] Sébastien Tanzilli, Hugues De Riedmatten, Wolfgang Tittel, Hugo Zbinden, Pascal Baldi, Marc De Micheli, Daniel Barry Ostrowsky, and Nicolas Gisin. Highly efficient photon-pair source using periodically poled lithium niobate waveguide. *Electronics Letters*, 37(1):26–28, 2001.

[37] Kaoru Sanaka, Karin Kawahara, and Takahiro Kuga. New high-efficiency source of photon pairs for engineering quantum entanglement. *Physical Review Letters*, 86(24):5620, 2001.

[38] Konrad Banaszek, Alfred B U'Ren, and Ian A Walmsley. Generation of correlated photons in controlled spatial modes by downconversion in nonlinear waveguides. *Optics letters*, 26(17):1367–1369, 2001.

[39] Simone Ferrari, Carsten Schuck, and Wolfram Pernice. Waveguide-integrated superconducting nanowire single-photon detectors. *Nanophotonics*, 7(11):1725–1758, 2018.

[40] Jianwei Wang, Stefano Paesani, Yunhong Ding, Raffaele Santagati, Paul Skrzypczyk, Alexia Salavrakos, Jordi Tura, Remigiusz Augusiak, Laura Mančinska, Davide Bacco, et al. Multidimensional quantum entanglement with large-scale integrated optics. *Science*, 360(6386):285–291, 2018.

[41] Vinicius S Ferreira, Gihwan Kim, Andreas Butler, Hannes Pichler, and Oskar Painter. Deterministic generation of multidimensional photonic cluster states with a single quantum emitter. *arXiv preprint arXiv:2206.10076*, 2022.

[42] Peter J Shadbolt, Maria R Verde, Alberto Peruzzo, Alberto Politi, Anthony Laing, Mirko Lobino, Jonathan CF Matthews, Mark G Thompson, and Jeremy L O'Brien. Generating, manipulating and measuring entanglement and mixture with a reconfigurable photonic circuit. *Nature Photonics*, 6(1):45–49, 2012.

[43] Jacques Carolan, Christopher Harrold, Chris Sparrow, Enrique Martín-López, Nicholas J Russell, Joshua W Silverstone, Peter J Shadbolt, Nobuyuki Matsuda, Manabu Oguma, Mikitaka Itoh, et al. Universal linear optics. *Science*, 349(6249):711–716, 2015.

[44] Sara Bartolucci, Patrick Birchall, Hector Bombin, Hugo Cable, Chris Dawson, Mercedes Gimeno-Segovia, Eric Johnston, Konrad Kieling, Naomi Nickerson, Mihir Pant, Fernando Pastawski, Terry Rudolph, and Chris Sparrow. Fusion-based quantum computation. *arXiv preprint 2101.09310*, 2021.

[45] Fabian Ewert and Peter van Loock. 3/4-efficient bell measurement with passive linear optics and unentangled ancillae. *Physical review letters*, 113(14):140403, 2014.

[46] Anne Broadbent and Elham Kashefi. Parallelizing quantum circuits. *Theoretical computer science*, 410(26):2489–2510, 2009.

[47] Aleks Kissinger and John van de Wetering. Pyzx: Large scale automated diagrammatic reasoning. *arXiv preprint arXiv:1904.04735*, 2019.

[48] Gushu Li, Yufei Ding, and Yuan Xie. Tackling the qubit mapping problem for nisq-era quantum devices. In *Proceedings of the Twenty-Fourth International Conference on Architectural Support for Programming Languages and Operating Systems*, pages 1001–1014, 2019.

[49] Aric Hagberg, Pieter Swart, and Daniel S Chult. Exploring network structure, dynamics, and function using networkx. Technical report, Los Alamos National Lab.(LANL), Los Alamos, NM (United States), 2008.

[50] Maurizio Patrignani. On the complexity of orthogonal compaction. *Computational Geometry*, 19(1):47–67, 2001.

[51] Steven A Cuccaro, Thomas G Draper, Samuel A Kutin, and David Petrie Moulton. A new quantum ripple-carry addition circuit. *arXiv preprint quant-ph/0410184*, 2004.

[52] Michael Norman, Vince Kellen, Shava Smallen, Brian DeMeulle, Shawn Strande, Ed Lazowska, Naomi Alterman, Rob Fatland, Sarah Stone, Amanda Tan, et al. Cloudbank: Managed services to simplify cloud access for computer science research and education. In *Practice and Experience in Advanced Research Computing*, pages 1–4. 2021.